

Received October 6, 2020, accepted October 19, 2020, date of publication October 23, 2020, date of current version November 9, 2020.

Digital Object Identifier 10.1109/ACCESS.2020.3033381

# Surface Deformation Retrieving Over Soft Clay Based on an Improved Time Series InSAR Model: A Case Study of Dongting Lake Area, China

YIKAI ZHU<sup>1,2</sup>, XUEMIN XING<sup>1,2</sup>, ZHIHUI YUAN<sup>1,3</sup>, (Member, IEEE),  
LIANG BAO<sup>1,2</sup>, LINGJIE ZHU<sup>1,2</sup>, AND LIFU CHEN<sup>1,3</sup>

<sup>1</sup>Laboratory of Radar Remote Sensing Applications, Changsha University of Science and Technology, Changsha 410014, China

<sup>2</sup>School of Traffic and Transportation Engineering, Changsha University of Science and Technology, Changsha 410014, China

<sup>3</sup>School of Electrical and Information Engineering, Changsha University of Science and Technology, Changsha 410014, China

Corresponding author: Xuemin Xing (xuemin.xing@csust.edu.cn)


This work was supported in part by the National Natural Science Foundation of China under Grant 42074033, Grant 41701536, Grant 61701047, and Grant 41674040; in part by the Natural Science Foundation of Hunan Province under Grant 2017JJ3322 and Grant 2019JJ50639; in part by the Key Project of Education Department of Hunan Province under Grant 18A148; in part by the Project of Education Department of Hunan Province under Grant 16C0034; in part by the Open Fund of Engineering Laboratory of Spatial Information Technology of Highway Geological Disaster Early Warning in Hunan Province under Grant kfj190601; and in part by the Graduate Student Research Innovation Fund of Changsha University of Science and Technology under Grant CX2020SS10.

**ABSTRACT** The infrastructures built on soft clay in the Dongting Lake area are more prone to settlement and instability due to its significant rheological properties. It is of great importance to conduct a long-term surface deformation monitoring over this area. The most commonly used Synthetic Aperture Radar Interferometry (InSAR) deformation models are based on combinations of one or several pure empirical mathematical functions without considering the physical and mechanical characteristics of the observed objects. In this work, we propose an improved deformation model based on the functional relationship between strain and time in the Maxwell rheological model. The rheological parameters of elastic modulus and viscosity are introduced into a traditional empirical seasonal model. The improved model is applied for the investigation of the spatial-temporal surface evolution over the Dongting Lake area with the Small Baseline Subset InSAR (SBAS-InSAR) technology and TerraSAR-X satellite imagery. With the proposed model, the rheological parameters and the time series deformation are estimated, with the maximum accumulated subsidence estimated as 38 mm. Through the analysis of the generated results, we find that the lower the viscosity and elastic modulus are, the higher the deformation is. Temporally, the overall deformation follows a generally subsiding trend with a seasonal recovery of 5 mm from October 2012 to November 2012 and 12 mm from January 2013 to February 2013. To compensate for the deficiency of the unavailability of external geodetic measurements over this area, three different accuracy indexes (residual phase, temporal coherence, and high-pass deformation) are utilized to evaluate the modeling accuracy. The results of the improved model are also compared to three traditional models (seasonal model, cubic polynomial model, and linear model). The comparison shows that the improved model is highly recommended in this area because of its better accuracy.

**INDEX TERMS** InSAR, deformation, soft clay, Maxwell model, rheology, highway.

## I. INTRODUCTION

Soft clay is a kind of fine-textured soil most deposited at lake area, seashore, and riverbank. The geotechnical characteristics of soft clay are mainly high compressibility,

The associate editor coordinating the review of this manuscript and approving it for publication was Stefania Bonafoni .

low shearing resistance, high natural water content, small natural density, large void ratio, and low permeability [1]. Due to its geotechnical characteristics, the infrastructures (i.e. highways, buildings, and bridges) built on soft clay are more prone to settlement and instability, especially under high traffic loads. Therefore, it is of great significance to conduct long-term ground subsidence monitoring for the

infrastructures built on soft clay areas (i.e. lake area) [2]. MT-InSAR technology (Multi-temporal Interferometric Synthetic Aperture Radar) is a rapidly developed earth observation technique [3], which detects and estimates the interested ground deformation information through processing multi-temporal SAR (Synthetic Aperture Radar) images over those high-quality points. This technique, represented by Permanent Scatterer Interferometry (PSI) [4], Small Baseline Subset (SBAS) [5], [6], Temporally Coherent Point InSAR (TCP-InSAR) [7], SqueeSAR [8], and so on, has been proven to possess great capacities for monitoring large transportation infrastructures [9]–[11]. They can detect the information of ground displacement with submillimeter accuracy [12], which is a great complement to traditional monitoring measurements.

In the procedure of MT-InSAR data processing, deformation modeling is a key step to determine the temporal relationship between the phase component of displacement and the unknown deformational parameters. Earlier studies proved that the deformation model can strictly influence the accuracy of the final estimated deformation [13]. The most commonly used InSAR deformation models are based on the combinations of one or several pure empirical mathematical functions to fit the physical process of deformation evolution with time (i.e. linear model, seasonal model, polynomial model, and hyperbola models), which ignore the physical and mechanical characteristics of the monitored object [14]–[16]. The parameters for those empirical models are generally mathematical coefficients without certain mechanical significance, which show limitations in both the accuracy of deformation estimation and the subsequent deformation interpretation. Considering the deficiency of the aforementioned models, the deformation mechanisms of the observed objects are considered and introduced into traditional models in recent years, which have been successfully applied in the deformation investigation induced by permafrost [17], [18], mining activities [19], thermal expansions [20]. For those models, the parameters reflecting the physical characteristics or the external environmental variations are introduced in the time series modeling. The successful experimental results based on those physical models proved that, with consideration of the deformation mechanism, the temporal variations can be better described, and the accuracy of the estimated deformation can be highly improved.

Previous research results also showed that the surface deformation of soft clay subgrade is prone to seasonal factors (such as temperature and precipitation) [21]. The deformation of soft clay materials can be divided into three stages in temporal evolution: instantaneous, primary consolidation, and secondary consolidation [22]. The secondary consolidation is the main settlement component during the operation step of the highway post-construction. During this stage, the underground deformation increases with time under a constant external load, hence the dominant deformation is related to the rheological characteristics of soil [23], [24].

The rheological property is a significant engineering property of soft clay, which describes the temporal effect that the deformation of soils increases with time under a constant load [25]. The rheological parameters (i.e. elastic modulus and viscosity) are primary factors for representing the rheological properties. The rheological model, which describes the dynamic temporal variations, can quantitatively represent the functional relationship between the strain of soft soil material and the rheological parameters. The most commonly used rheological models are mainly based on the series-parallel connection of basic mechanical components (i.e., Kelvin model, Maxwell model, and Burgers model), which can easily express the complex rheological properties of the soft soil. Since the Maxwell model has been proved applicable in the simulation of the initial or stable rheological deformation of soil material [17], [26], we attempt to introduce it into the traditional seasonal model during the process of deformation modeling.

Based on the background discussed above, we presented an improved deformation model combining the one-dimensional rheological Maxwell model and seasonal model. The improved model is utilized to describe the temporal variations for the deformation of soft clay [27]–[29]. Dongting Lake area is selected as the study area in our work. SBAS-InSAR technology and TerraSAR-X imagery are utilized to generate the time series deformation results over the soft clay along the YanHu Highway (YH) and its surrounding area. The model parameters were estimated through the Genetic Algorithm (GA) combined with the Simplex Method. Three different accuracy indexes (residual phase, temporal coherence, and HP deformation) were utilized to evaluate the final accuracy. A comparative analysis based on four different types of deformation models, including the conventional Linear Model (LM), the Cubic Polynomial Model (CPM), the Seasonal Model (SM), and the Improved Model (IM) was executed to reflect the effect of the IM. Furthermore, temporal deformation characteristics over feature points and the rheological properties contributing to land subsidence were analyzed in detail. Finally, a sensitivity analysis between the IM parameters and the generated subsidence was carried out.

## II. METHODS

### A. TRADITIONAL MODELS USED IN SBAS-InSAR TECHNOLOGY

Firstly, assume that  $N+1$  SAR images covering the same area are acquired at dates  $(t_0, \dots, t_n)$  and all the images have been registered in the same coordinate system. Then  $M$  interferometric pairs with spatial-temporal baseline less than a certain threshold can be obtained through two-orbit Differential InSAR (DInSAR) processing, where  $M$  satisfies the inequality  $\frac{N+1}{2} \leq M \leq N(\frac{N+1}{2})$ . Subsequently, phase unwrapping will be executed and an external DEM will be used to remove the topographic phase for each interferometric pair. The unwrapped phase at pixel  $(x, y)$  in the  $i$ th interferogram with the period from dates  $t_A$  to  $t_B$  ( $t_B > t_A$ ) can be

expressed as [17]:

$$\begin{aligned} \delta\phi_i(x, y) &= \phi(t_B, x, y) - \phi(t_A, x, y) \\ &= \Delta\phi_{def}^i(t_B, t_A, x, y) + \frac{4\pi}{\lambda} \frac{B_{\perp} \Delta z(x, y)}{r \sin \theta} + \Delta\phi_{res}^i(x, y) \end{aligned} \quad (1)$$

where  $i \in (1, \dots, n)$  represents the order number of interferograms;  $(x, y)$  is the SAR coordinates along the range and azimuth direction;  $\phi(t_B, x, y)$  and  $\phi(t_A, x, y)$  are phase value of two SAR images;  $\Delta\phi_{def}^i$  defines the low-pass (LP) phase component throughout the  $i$ th interferogram;  $B_{\perp i}$  defines the spatial baseline;  $\Delta z$  represents the residual elevation;  $r$  is the range between the sensor and ground object;  $\theta$  is the incidence angle and  $\lambda$  is the radar wavelength.  $\Delta\phi_{res}^i$  defines the residual phase component, which is related to noise, atmospheric delay, and high-pass (HP) deformation.

The linear deformation model assumes that the displacement for each time-adjacent interferometric period follows linearly variation. The functional relationship between deformation and subsidence rate can be written as:

$$\begin{aligned} \Delta\phi_{def}^i &= \frac{4\pi}{\lambda} \Delta D_{def}^j \\ &= \frac{4\pi}{\lambda} \sum_{i=j+1}^k v_i(t_i - t_{i-1}) \end{aligned} \quad (2)$$

where  $\Delta D_{def}^j$  defines the LP deformation throughout the  $i$ th interferogram;  $j$  and  $k$  represent the indexes of the master image at the date  $t_A$  and slave image at the date  $t_B$ , respectively. In contrast, the seasonal model supposes  $\Delta\phi_{def}^i$  as consisting of linear and periodic subsidence, which has been widely used in describing the deformation related to seasonal factors. For the seasonal model,  $\Delta\phi_{def}^i$  can be expressed as [15], [30]:

$$\begin{aligned} \Delta\phi_{def}^i &= \frac{4\pi}{\lambda} \Delta D_{def}^j \\ &= \frac{4\pi}{\lambda} [a_1 t + a_2 \sin(\frac{2\pi}{T} t) + a_3 \cos(\frac{2\pi}{T} t)] \end{aligned} \quad (3)$$

where  $T$  defines the seasonal deformation period ( $T = 365$  days);  $a_1$ ,  $a_2$ , and  $a_3$  are the unknown parameters.

### B. THE IMPROVED MODEL BASED ON MAXWELL RHEOLOGICAL MODEL

As discussed in section I, an improved deformation model combining the one-dimensional rheological Maxwell model and the seasonal model will be built as follows. Fig. 1 shows the schematic diagram of the combined elements in the Maxwell rheological model, which is a series-connected system with a spring (pure elastomer) and a glue pot (pure viscous body). The Maxwell model can better describe the physical deformation process of viscoelasticity objects (i.e. soft soil), and illustrate the phenomenon that the instantaneous elastic deformation will be restored immediately after the unloading of the soil. The rheological response presented by the Maxwell model is between elastic solid and



FIGURE 1. Maxwell rheological model ( $\sigma_c$  defines the external load which is regarded as constant;  $E$  and  $\eta$  represent the elastic modulus and the viscosity coefficient, respectively).

viscous fluid. The rheological constitutive equation of the Maxwell model can be expressed as [31]:

$$\varepsilon = \frac{\sigma_c}{E} + \frac{\sigma_c}{\eta} t \quad (4)$$

where  $\varepsilon$  is the strain caused by material;  $\sigma_c$  defines the external load which is regarded as an invariant value;  $E$  and  $\eta$  represent the elastic modulus and the viscosity coefficient, which are two of the most significant rheological parameters;  $t$  is the total period of the strain occurrence. Among them,  $E$  and  $\eta$  are unknown parameters. The strain expressed in (4) is composed of two parts: 1) the instantaneous elastic deformation, which is a time-unrelated component, keeps constant during the total temporal period; 2) the stable creeping component, which is a time-related component, increases with the time.

The total structure of the highway can be divided into the pavement layer, subgrade layer, and soft clay subgrade layer. The influence between the surface deformation and the settlement of the soft clay subgrade is mainly focused on in this work. The functional relationship between the subsidence of the soft clay subgrade and the strain can be expressed as [25]:

$$S = \int_{t_A}^{t_B} \int_0^H \varepsilon \cdot dh dt \quad (5)$$

where  $S$  represents the subsidence along the vertical direction;  $t_A$  and  $t_B$  represent the start time and the end time of the strain occurrence, respectively;  $H$  defines the average thickness of the soft clay subgrade which can be obtained from the highway design materials. Combining (4) and (5),  $S$  can be written as:

$$S = \frac{H\sigma_c}{E^2} (t_B - t_A) + \frac{H\sigma_c}{2\eta} (t_B^2 - t_A^2) \quad (6)$$

Substituting (3) and (6) into (1), it can be written as:

$$\begin{aligned} \delta\phi_i(x, y) &= \phi(t_B, x, y) - \phi(t_A, x, y) \\ &= \frac{4\pi \cos \theta}{\lambda} \left[ \frac{H\sigma_c}{E^2} (t_B - t_A) \right. \\ &\quad + \frac{H\sigma_c}{2\eta} (t_B^2 - t_A^2) + a_1(t_B - t_A) \\ &\quad + a_2(\sin(\frac{2\pi}{T} t_B) - \sin(\frac{2\pi}{T} t_A)) \\ &\quad + a_3(\cos(\frac{2\pi}{T} t_B) - \cos(\frac{2\pi}{T} t_A))] \\ &\quad + \frac{4\pi}{\lambda} \frac{B_{\perp} \Delta z(x, y)}{r \sin \theta} + \Delta\phi_{res}^i(x, y) \end{aligned} \quad (7)$$

For  $M$  generated interferometric pairs, the unknown parameters in (7) includes the rheological parameters  $E$  and  $\eta$ , seasonal parameters  $a_1$ ,  $a_2$ , and  $a_3$ , and the elevation correction  $\Delta Z$ . Theoretically, if there are at least six interferometric pairs, the unknown parameters over all the high coherence points of each image can be solved. Consequently, the corresponding rheological parameters can be estimated.

### C. UNKNOWN PARAMETERS ESTIMATION

It is a nonlinear multi-parameter estimation problem to estimate the 6 unknown parameters:  $E$ ,  $\eta$ ,  $a_1, a_2, a_3$ , and  $\Delta z$ . The Genetic Algorithm (GA) for nonlinear Least-Squares estimation is utilized here to solve the unknown parameters. GA is a highly parallel, random, and adaptive optimization algorithm based on the principles of “survival of the fittest”, which has the advantages of simple principle, strong currency, unrestricted constraints, implicit parallelism, and global solution searching ability. The basic idea of GA is to obtain the population individuals as the final solutions of parameters, which can satisfy the condition of minimum fitness function through the operation of selection, crossover, and mutation [32]. The population size, iteration times, and the magnitude of the individual genes should be set preliminarily. As discussed in section II-B, each gene of a population includes the six parameters  $[E, \eta, a_1, a_2, a_3, \Delta z]$ . The fitness function is mainly modeled following the residual minimum norm principle, which can be expressed as follows:

$$f = \left\| \Delta \phi_{res}^i \right\| = \min \quad (8)$$

where  $\Delta \phi_{res}^i$  represents the residual phase in (7). As proposed in [19], the Simplex Method can help to improve the accuracy of GA generated solutions, hence we introduce it to optimize the searching results. The parameters obtained by GA are taken as the input initial values of the Simplex Method, and the output optimized searching results are determined as the final solutions.

### III. SIMULATED EXPERIMENT

To verify the feasibility and reliability of the aforementioned improved model, a simulated experiment was designed and implemented. Through the investigation of the design data and the structural morphology of the test highways, the rheological parameters were set as  $E \in [0, 25]$  MPa;  $\eta \in [0, 15] \times 10^6$  MPa. s. The linear rate  $a_1$  was set within the interval  $[-0.15, 0.1]$  mm/yr, the periodical coefficients  $a_2$  and  $a_3$  within the range of  $[-0.15, 0.1]$  m/yr, whereas the elevation correction  $\Delta z$  within the range of  $[-50, 50]$  m. The spatial and temporal baselines in this simulation were set according to the TerraSAR-X sensor parameters in the real experiment. A total of ten interferometric pairs were generated. In the simulated experiment, 200 high coherence points were randomly generated, and the curved surface function was utilized to simulate the rheological parameters. The elevation correction was simulated with the two-dimensional Gaussian Function model. The values of those parameters for

each high coherence point were picked up from the simulated field as true values to verify the accuracy of the estimated coefficients.

Fig. 2 shows the comparison between the estimated value of rheological parameters and the real values (the noise level here was 0.5 rad). As shown in Fig. 2, the comparative results are in good consistency with the simulated real value. To quantitatively evaluate the accuracy of the simulation, the Root Mean Square Error (RMSE) of each unknown parameter at all the high coherence points is illustrated in TABLE 1. For the six unknown parameters, the magnitude of errors accounts for even lower than 4% of the mean parameter estimations, which implies the feasibility of the aforementioned model and the parameters estimation algorithm.

**TABLE 1. RMSE Comparison for each parameter in the simulated experiment.**

Rheological parameters	RMSE
$E$ (MPa)	$\pm 0.4728$ (2.0%)
$\eta$ ( $10^6$ MPa.s)	$\pm 0.2427$ (1.6%)
$a_1$ (m/yr)	$\pm 0.0081$ (3.2%)
$a_2$ (m/yr)	$\pm 0.0042$ (1.7%)
$a_3$ (m/yr)	$\pm 0.0033$ (1.3%)
$\Delta z$ (m)	$\pm 0.7887$ (2.7%)

## IV. EXPERIMENT OVER DONGTING LAKE AREA

### A. STUDY AREA

Dongting Lake is located in the South Bank of the Yangtze River in the north of Hunan Province, which is a tectonic lake with the characteristics of a barrier lake. With a well-developed surrounding water system, Dongting Lake is adjacent to the Yangtze River to the north, with its river water flowing into the Xiang River. Yueyang is a lakeside city of Hunan Province next to Dongting Lake, which is under the combined geological structure characteristics of intermittent uplift denudation and intermittent stable uplift sedimentation. As a city with a population of 5.8 million, plenty of residential areas and developed transportation network are distributed in Yueyang. Every flood season, the residential areas around Dongting Lake are under potential danger of accumulated deformation, ground surface collapse and even landslides of the slope. The stability control of the densely distributed infrastructures near the Lake area is of great importance.

The soft clay distributed in the Dongting Lake region belongs to lacustrine sedimentation, which is formed in a relatively still water environment. It experienced two sedimentary cycles, showing a certain range of lenticles (such as clay soil) in the stratigraphic structure [33], [34]. Soft clay generally contains a thin layer of silty sand and fine-silty sand with various thicknesses, which is one of the primary objects for subgrade treatment. The soft clay in this area is mainly composed of silt, mucky clay, and soft plastic clay, and shows the characteristics of high water content, high void ratio, large liquid index, strong compressibility, low shear strength, and

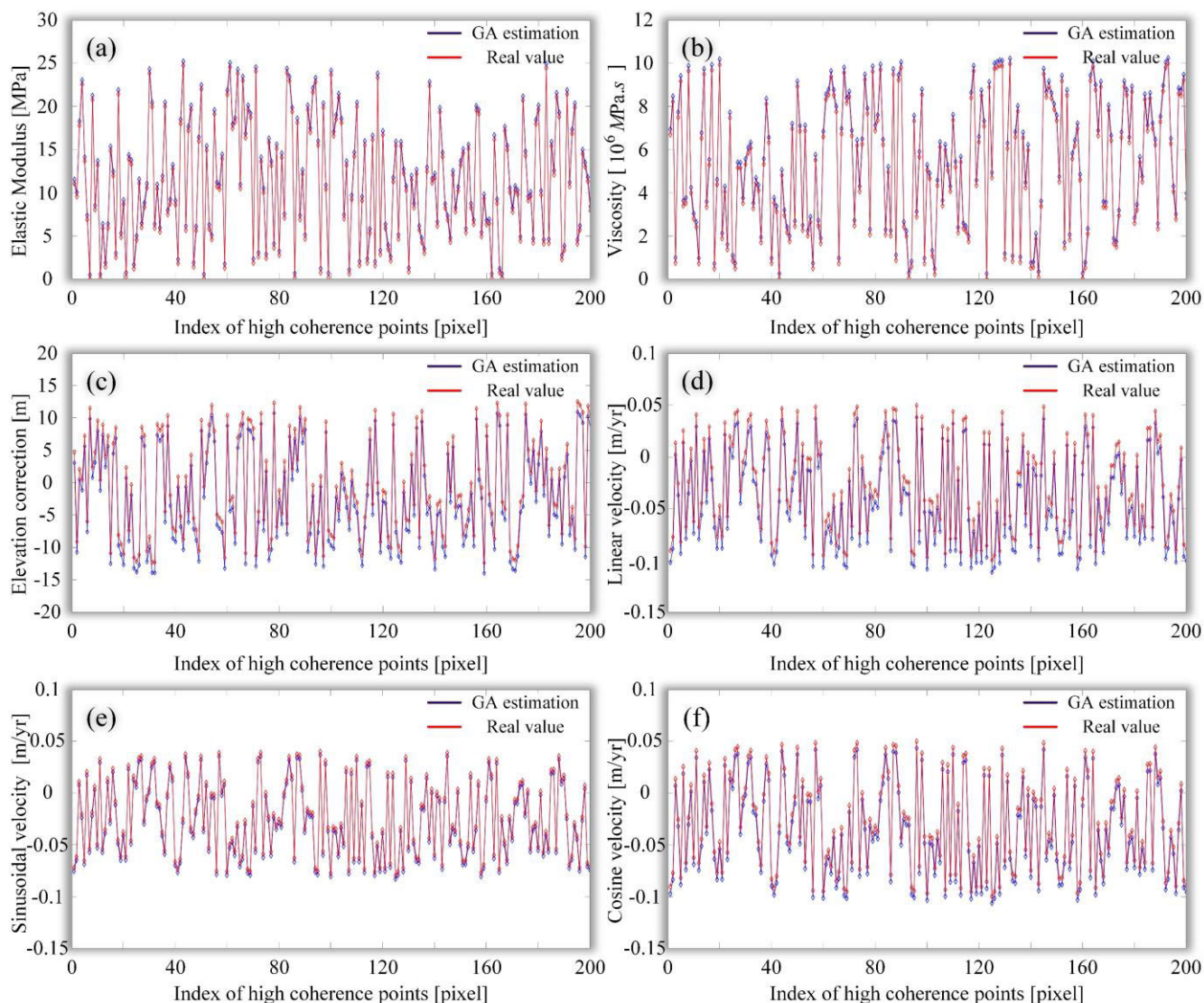


**FIGURE 2.** Estimated unknown parameters compared with real values in simulation (the noise level is 0.5 rad, X-axis represents the index of simulated high coherence points, and Y-axis defines the value of each parameter): (a) Elastic modulus  $E$ ; (b) Viscosity  $\eta$ ; (c) Elevation error  $\Delta z$ ; (d) Linear velocity  $a_1$ ; (e) Sinusoidal velocity  $a_2$ ; (f) Cosine velocity  $a_3$ .

low cohesion. Under the poor engineering properties and the vibration load, soft clay is vulnerable to lateral slip, uneven settlement and creep, which can impose a negative impact on the stability of subgrade.

The Yanhu Highway (YH) along the Dongting Lake is selected as the main study object. We carried out real data experiments over YH and its surrounding areas (including the urban area of Yueyang City). YH is one of the main channels from the urban area to Chenglingji port, and also an important part of the scenic belt along the lake in Yueyang central urban area, which connects Dongting Lake Bridge, Dongting Lake Super Bridge, Hangrui Expressway, and other important infrastructures. The width of the carriageway is 24m with a two-way six-lane asphalt concrete pavement. The spatial coverage of the selected TerraSAR-X image is outlined by the

outside yellow rectangles in Fig. 3a, while the inside yellow rectangle is a subset of the differential interferometry selected in this experiment. The location of YH with the external DEM as the background is shown in Fig. 3b. The territory of China is shown in Fig. 3c. As shown in Fig. 3, YH is located next to Dongting Lake, built on a complete soft clay subgrade under large traffic volume.

Dongting Lake area is located in the East-Asian monsoon climate zone, under the transitional nature of the mid-subtropical zone to the north subtropical zone. The climate of the area belongs to the humid continental monsoon climate, which is especially uniform in the lake areas, with the characteristics of sufficient precipitation and strong seasonality. The annual average temperature over the area is 16.4 °C to 17 °C [35].

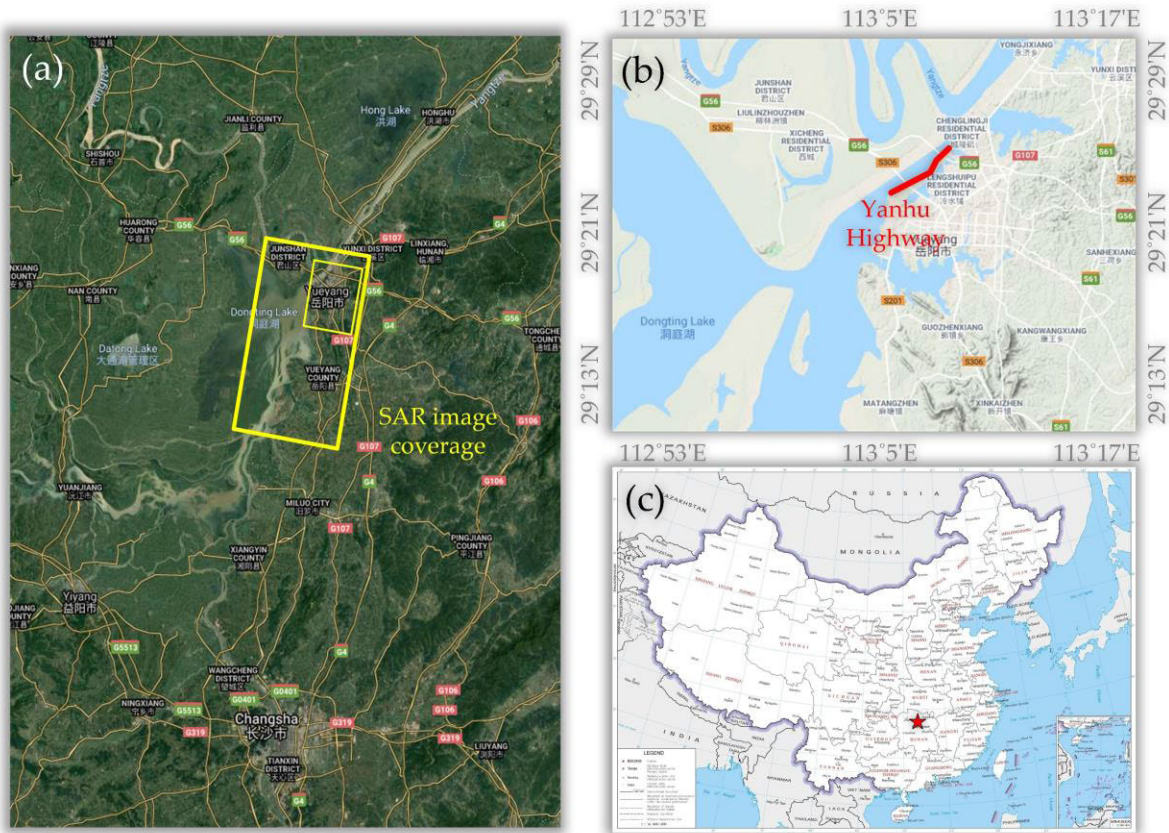


**FIGURE 3.** Study area featured at different scales: (a) the TerraSAR-X image coverage; (b) the location of YH; (c) the location of the study area in China map.

## B. DATA USED

The TerraSAR-X sensor was launched on June 21, 2007, which operated in the X-band of HH, VV, HV, and VH polarization modes [36]. A total of 24 repeat-pass TerraSAR-X Stripmap descending images, covering the period from December 28, 2011, to April 3, 2013, were available and collected in this work. The tracking number is 011 and the incident angle is  $39.23^\circ$ . The detailed parameters of these TerraSAR-X images are listed in TABLE 2. A 1-arc-second Shuttle Radar Topography Mission Digital Elevation Model (SRTM DEM) with the 30-m resolution provided by NASA was used to remove the topography-related phase. To better interpret the mechanism of surface deformation, the monthly average temperature, and precipitation data from December 2011 to April 2013 were collected in this work [37].

## C. DATA PROCESSING

ENVI 5.2 and SARscape 5.3 software were applied to conduct the interferometric process. SBAS processing was used to generate the unwrapped interferograms. The thresholds for the spatial-temporal baselines of the interferometric combination were empirically set to 120 m and 300 days, respectively. In total, 243 small baseline interferograms were

generated. The spatial-temporal baselines of each interferometric pair are shown in Fig. 4. The topographic phase was removed by utilizing the SRTM 1-arc-second DEM ( $\sim 30$  m spacing) from the National Aeronautics and Space Administration (NASA). The multi-look ratio was set as 2:2 in our experiment. Also, the Goldstein filter was applied to suppress the noise phase and a polynomial fitting method was selected to eliminate the orbit error. Then, the commonly used Minimum Cost Flow (MCF) algorithm was utilized for the phase unwrapping [38]. After eliminating the interferometric pairs with low quality, a total of 42 interferometric pairs were obtained.

The following steps, including high coherence points identification, deformation modeling, and unknown parameter estimation, were all performed with Matlab software. For the sake of improving the quality of coherence points, we selected the high coherence points based on the following criteria: 1) the average coherence value higher than 0.85; 2) the amplitude deviation index lower than 0.2; 3) the intensity value higher than 0.5 [39]. Consequently, 1329 high coherence points were extracted from the candidates. The improved model based on the Maxwell rheological model and the seasonal model discussed in Section II was used to model the temporal function between the unwrapped phase and the

**TABLE 2.** List of the interferometric pairs and their parameters with image No. 7 as the super master image (Orbit No. 11, descending).

Image No.	Acquisition Date (yyyy/mm/dd)	Normal Baseline (m)	Temporal Baseline (days)
0	2011/12/28	-146.49	319
1	2012/02/10	-78.42	275
2	2012/03/03	-152.67	253
3	2012/03/25	-68.99	231
4	2012/04/16	-17.04	209
5	2012/05/08	7.36	187
6	2012/05/30	6.76	165
7	2012/08/26	10.48	77
8	2012/09/17	-51.35	55
9	2012/10/09	-196.91	22
10	2012/10/31	-37.39	11
11	2012/11/11	0	0
12	2012/11/22	-83.01	11
13	2012/12/14	92.09	33
14	2012/12/25	-49.65	44
15	2013/01/05	-122.19	55
16	2013/01/16	-89.49	66
17	2013/01/27	-146.08	77
18	2013/02/07	18.77	88
19	2013/02/18	-98.52	99
20	2013/03/01	-258.87	110
21	2013/03/12	-172.26	121
22	2013/03/23	81.71	132
23	2013/04/03	-177.08	143

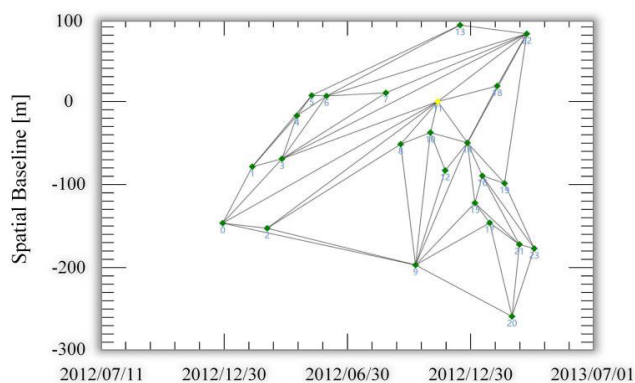


**FIGURE 4.** Spatial-temporal baselines of each interferometric pair (X-axis defines the acquisition dates of SAR images; Y-axis defines the perpendicular baselines; the yellow rhombus represents the super master image).

deformation parameters, and the unknown parameters were estimated through GA. Consequently, the unknown deformation parameters, including the rheological coefficients, were estimated, and the corresponding LP deformation component was obtained [32], [40], [41]. To extract the HP deformation component, the residual phase was filtered with a temporally HP filtering and spatially LP filtering [17]. Finally, the total deformation was obtained by adding the HP and the LP deformation component at each pixel.

**V. EXPERIMENTAL RESULTS**

**A. ESTIMATED MODEL PARAMETERS OF THE IMPROVED MODEL**

The estimated parameters for the improved model at each high coherence point are shown in Fig. 5 (with the

topographic map as the background). The elastic modulus and viscosity are shown in Fig. 5a and 5b, respectively. As it shows, the value of the elastic modulus is mainly distributed in the interval [0, 28] MPa, whereas the value of viscosity varies from 0 MPa.s. to  $7 \times 10^6$  MPa.s. From the spatial distribution, the magnitude of rheological parameters is generally following the characteristic of higher for the inland area and lower for the coastal area, with the color ranging from light green to heavy red. For instance, the estimated rheological parameters of point B (located in the coastal area) are 15.2 MPa and  $2.2 \times 10^6$  MPa.s, while those of point C (located in the inland area) are 26.3 MPa and  $7.2 \times 10^6$  MPa.s. According to our in-situ investigation, the sedimentary lacustrine soil distributed in this area mainly contains typical clay and muddy clay [42]. Earlier studies based on the indoor one-dimensional consolidation rheological tests for the soil properties around the Dongting Lake area showed that: the soil along the lake was mainly mucky clay and mild clay, with the magnitude of the elastic modulus in the interval [0, 12] MPa and the viscosity within the interval  $[0, 4] \times 10^6$  MPa.s; the soft clay layer of the inland area was mainly composed of mealy sand and mucky clay, with the elastic modulus value distributed in the interval [15], [25] MPa and the viscosity was within the interval  $[5], [8] \times 10^6$  MPa.s. The results show good agreement with the estimated magnitude of the rheological parameters in our work [43]–[45]. Besides, we found that the lower the rheological parameters value is, the higher the deformation is (which will be discussed in section VI in detail). Accordingly, the magnitude of the estimated elastic modulus and viscosity parameters in our experiment can reflect the spatial-temporal deformation characteristics over this area.

Parameters, including linear velocities and periodical coefficients, are shown in Fig. 5c-e, respectively. According to our estimations, the sinusoidal velocity  $a_2$  ranges from -2 mm/yr to 0 mm/yr, the cosine velocity  $a_3$  from -3 mm/yr to 0 mm/yr, and the linear velocity  $a_1$  from -6 mm/yr to -1 mm/yr. The estimated elevation error  $\Delta z$  is shown in Fig. 5f, which is mainly distributed between -10 m and 8 m.

**B. OVERALL TIME-SERIES DEFORMATION RESULTS**

The overall time series deformation from December 28, 2011, to April 3, 2013, was generated based on the improved model, which is shown in Fig. 6. From the spatial distribution, the large subsiding area is generally distributed at the lake bank area, and expanding temporally from bank to inland area, which shows an inverse spatial distribution characteristic to Fig. 5 (which will be discussed in Section 6). The accumulated subsidence at YH road was -38 mm, whereas only -11 mm was located in the east-south inland area (shown in the first image of Fig. 6 with a purple rectangle). Temporally, from the color variations shown in Fig. 6, the overall deformation trend is subsidence. However, from October 31, 2012, to November 22, 2012, and January 27, 2013, to February 28, 2013, obvious jumps in the deformation occurred, with the maximum recovery of 12 mm (which will be discussed in

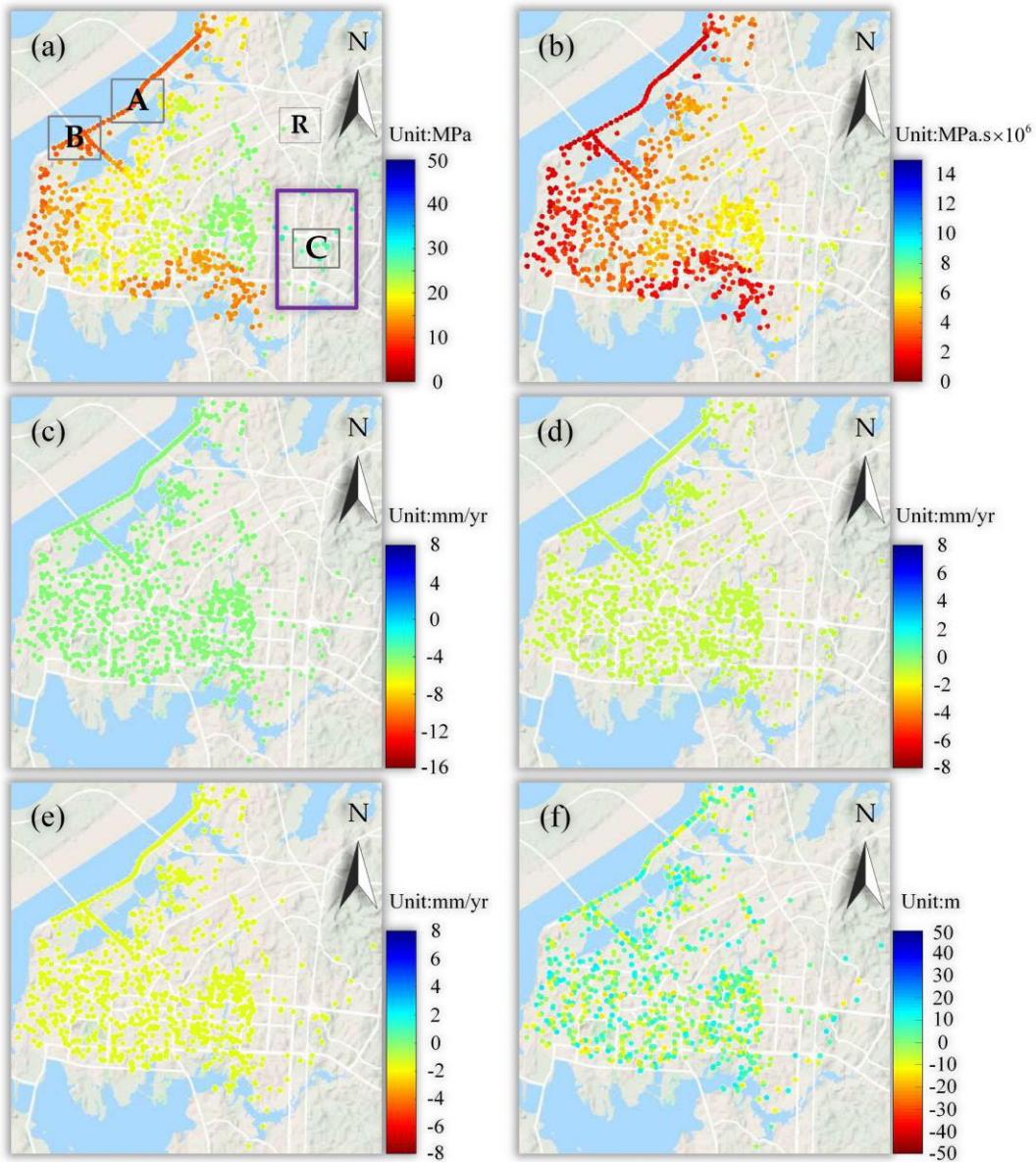


**FIGURE 5.** Estimated model parameters: (a) Elastic modulus  $E$ ; (b) Viscosity  $\eta$ ; (c) Linear velocity  $a_1$ ; (d) Sinusoidal velocity  $a_2$ ; (e) Cosine velocity  $a_3$ ; (f) Elevation error  $\Delta z$ .

Section VI in detail). According to our results, the peak subsidence accumulated up to 38 mm on April 3, 2013.

**C. ACCURACY EVALUATION**

The time-series deformation generated by the Improved Model (IM) was compared to three traditional models—the conventional Linear Model (LM), Cubic Polynomial Model (CPM), Seasonal Model (SM). To compensate for the unavailability of the external in-situ deformation measurements over this area, three different accuracy indexes (residual phase, temporal coherence, and HP deformation) were estimated for the four models:

1. three Residual Phase (RP): can be calculated by subtracting the LP phase component from the unwrapped phase series ( $\Delta\varphi_i^{res}(x, y)$  in (1)). This index indicates the fitting performance for each model [46], that is, the smaller the residual phase is, the higher the accuracy for the model selected. As shown in Fig. 7, the Root Mean Square (RMS) of the residual phase recovered from the four models is less than 0.7, indicating the feasibility for all the four models and SBAS technology in the applications of soft clay area. It can be seen from Fig. 7 that the IM shows the best performance, with the lowest RP phase for 42 interferograms. TABLE 3 lists the total RMS for



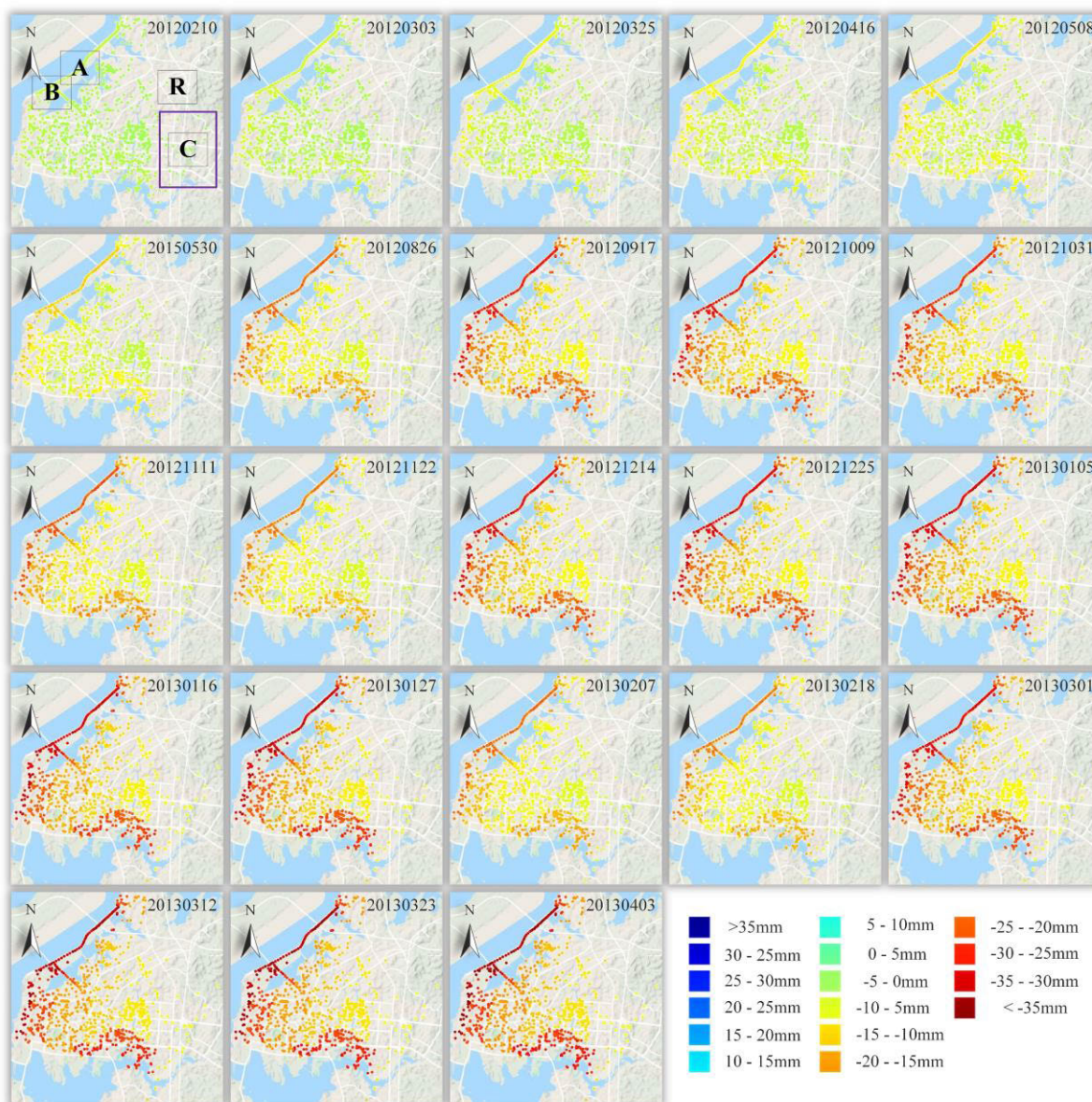


**FIGURE 6.** Time-series deformation based on the improved model with reference to 2011/12/28 (point A, B, and C are the selected typical points which will be discussed in detail in section VI; point R is the reference point).

four models. As shown in TABLE 3, both IM and SM have better performance, which means the temporal evolution of the surface deformation in the Dongting Lake area can be modeled more accurately by IM.

2. Temporal Coherence (TC): according to reference [18], the higher TC value implies higher modeling accuracy. From Fig. 8, it is obvious that IM shows the highest TC value (heavy yellow color for most of the high coherent points). The average TC value for each model is listed in the second row of TABLE 3, which quantitatively describes the performance for each model, in good agreement with Fig. 8.

3. HP deformation: As introduced in reference [47], the HP deformation component can also be used to assess the modeling accuracy besides the aforementioned indexes. As mentioned in 3.3, HP deformation can be estimated through a temporally HP filtering (the triangle filter method was utilized in our experiment) and spatially LP filtering (the mean filter method was utilized in our experiment). Fig. 9 shows the mean HP deformation of each interferogram generated by the four models. As it shows, all the HP deformation is lower than 6 mm for the four models. HP deformation obtained from the IM is lower than that of other models, indicating a higher fitting degree. The estimated RMS

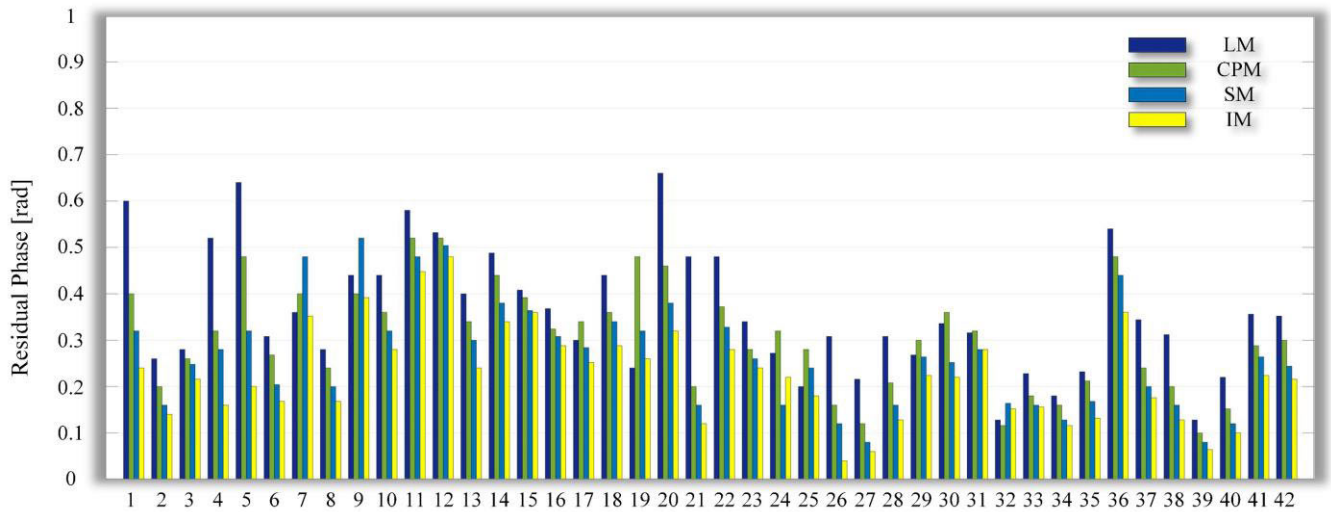


FIGURE 7. RMS of the residual phase for 42 interferograms generated by the four deformation models.

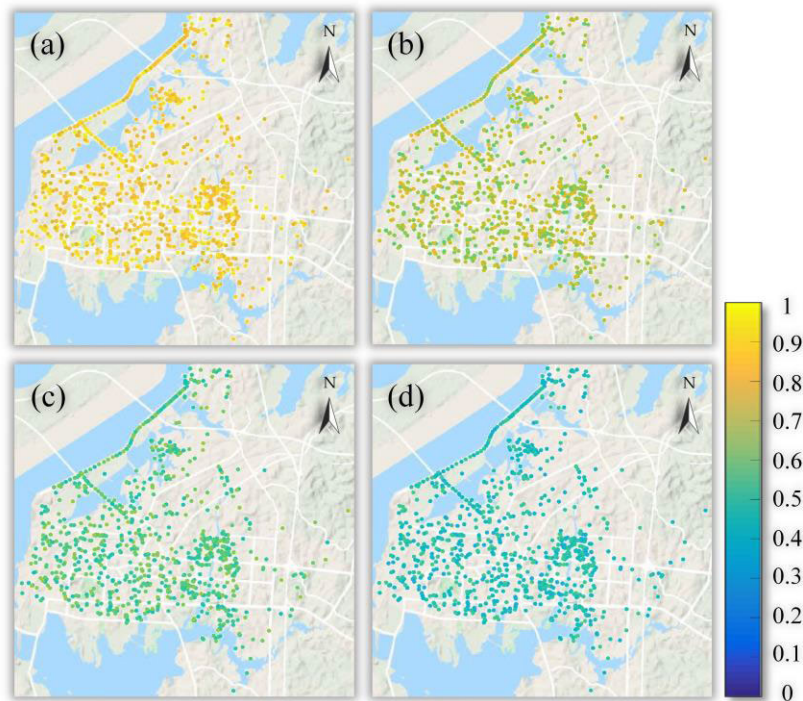


FIGURE 8. Mean Temporal Coherence for four deformation models: (a) IM; (b) SM; (c) CPM; (d) LM.

value of the temporal mean HP deformation is listed in TABLE 3.

VI. DISCUSSIONS

A. TEMPORAL DEFORMATION CHARACTERISTICS OVER FEATURE POINTS

Three feature points located in YH and Dongting Bridge (marked as A, B, and C in Fig. 6, the locations on the

optical images are shown in Fig. 10) were selected for further analysis. As shown in Fig. 10, A locates at the segment next to Dongfeng Lake of YH, whereas B at the junction of YH and Dongting Lake Bridge and C at X026 Road. Generally, for point A, the time series settlement showed a similar subsiding trend, with the maximum settlement of 28 mm occurred on April 3, 2013, for the LM-generated results, whereas 34 mm for that of IM. Comparatively, from

**TABLE 3. Quantitative comparison accuracy indexes for four models.**

Deformation Models	Mean TC value	RMS of HP Deformation (mm)	RMS of RP (rad)
IM	0.9525	0.6692	0.1004
SM	0.7824	0.7312	0.1129
CPM	0.7213	0.7762	0.1130
LM	0.6112	0.9843	0.1328

May 30, 2013, to October 31, 2013, accelerate subsiding occurred for the IM-generated results, whereas obvious uplifts with a recovery of 4 mm and 10 mm occurred during the periods from October 31, 2012, to November 22, 2012, and January 27, 2013, to February 18, 2013, respectively (marked as red arrows in Fig. 11). Similar temporal variation can be found at point B and C, with its subsidence magnitude slightly lower than that of point A. The maximum subsidence generated by LM accumulated to 26 mm for point B and 9 mm for point C, whereas 28 mm for the IM-generated results at point B and 11 mm at point C. According to the collected temperature and precipitation data, it is suggested that the uplift was related to the sudden increase of precipitation from October 31, 2012, to November 22, 2012, and January 27, 2013, to February 18, 2013, combined with the impact of the decrease of temperature, which will be discussed in VI-C. The evaporation of the underground water layer was far less than the external water supply, which lead to the phenomenon of uplift on the surface.

To more specifically describe the influence of rheological properties over this area, the proportion of each deformation component is shown in TABLE 4, TABLE 5, and TABLE 6, respectively. For point A, the isolated deformation component related to rheological properties accounted for 75% of the total deformation. The seasonal component accounted for 14%, and HP-deformation isolated from the residual component only accounted for 3%. This indicates that a large majority of the nonlinear deformation was detected by IM. In contrast, for the result generated by the pure LM, the linear component accounted for 78%, and the residual non-linear deformation only accounted for 22%. The result indicates that significant non-linear deformation has not been detected through pure LM. The IM can better model the temporal physical relationship between the real deformation and the physical parameters mechanically for the soft clay in this area.

**TABLE 4. Proportion of each deformation component at point A.**

Deformation Models	IM	LM
Rheological component	75%	0%
Seasonal component	14%	0%
Linear component	8%	78%
Residual component	3%	22%

**TABLE 5. Proportion of each deformation component at point B.**

Deformation Models	IM	LM
Rheological component	68%	0%
Seasonal component	18%	0%
Linear component	10%	77%
Residual component	4%	23%

**TABLE 6. Proportion of each deformation component at point C.**

Deformation Models	IM	LM
Rheological component	52%	0%
Seasonal component	25%	0%
Linear component	18%	80%
Residual component	5%	20%

**B. RHEOLOGICAL PROPERTIES CONTRIBUTING TO LAND SUBSIDENCE**

Rheological properties are the main engineering characteristic for the soil distributed in this area, and the soft clay for the roads are with the most significant rheological properties. Rheology is a time effect that describes the phenomenon that the deformation of materials increases with time under constant load. Under the action of the skeleton stress (effective stress), the soil particles show the characteristic of viscosity which is related to the adsorbed water (or gas) on the surface, so that the rearrangement of particles and the dislocation of the skeleton are highly related to time, that is, the temporal effect for deformation. The elastic modulus  $E$  can be simply defined as the stress divided by the strain along the direction. The viscosity  $\eta$  means the resistance to flow for a fluid, which can be understood as the ability to resist deformation. It can be inferred from (6) that the smaller the value of rheological parameters is, the larger the deformation is [48], [49]. Accordingly, the magnitude of the estimated elastic modulus and viscosity parameters in our experiment can reflect the spatial-temporal deformation characteristics over this area. It can be found from Fig. 5 and Fig. 6, that the inland area in the center part was under a relatively stable deformation, with higher elastic modulus and viscosity values. In contrast, the lake bank area showed significantly higher deformation and lower magnitude of elastic modulus and viscosity. As (5) shows, deformation can be understood as a combined temporal and spatial integration along the vertical direction of strain. Accordingly, when the external load is constant, the stress can be considered as a constant. It can be inferred that the higher the elastic modulus is, the lower the deformation is. Viscosity coefficient can be treated as a measure to describe the viscosity of a fluid, which is a demonstration of the fluid flow dynamics for its internal friction phenomenon [50]. Higher viscosity represents greater friction in the fluid. Therefore, viscosity is treated here as the parameter that demonstrates the internal friction property of soil mass and its ability to resist deformation. The higher the value of the viscosity is, the greater the friction resistance

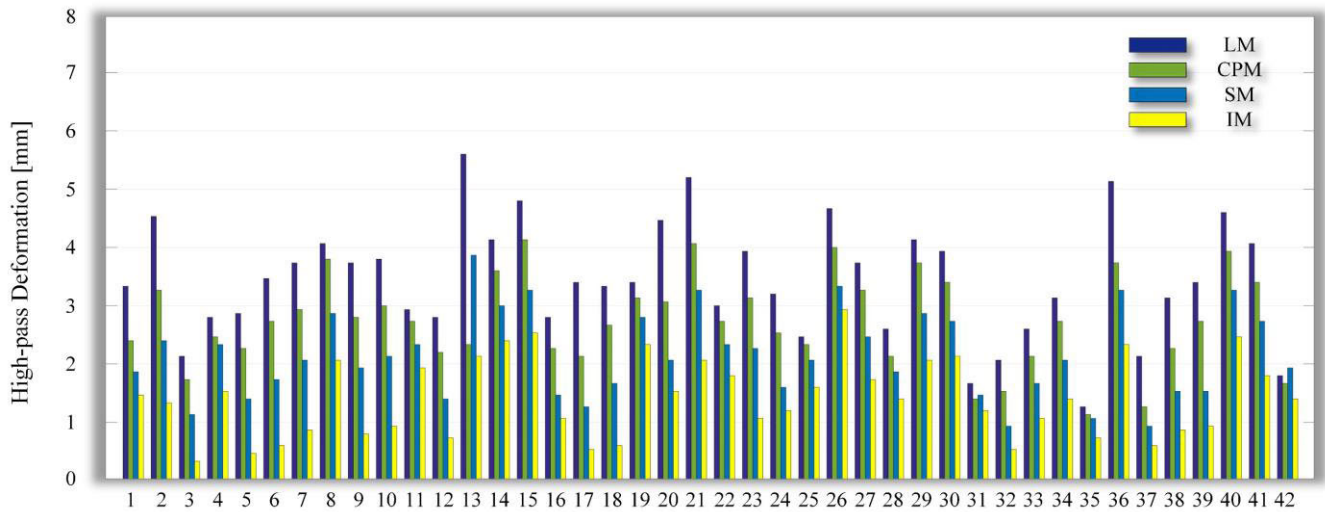


FIGURE 9. RMS of HP deformation of a 42-interferogram comparison for four models.

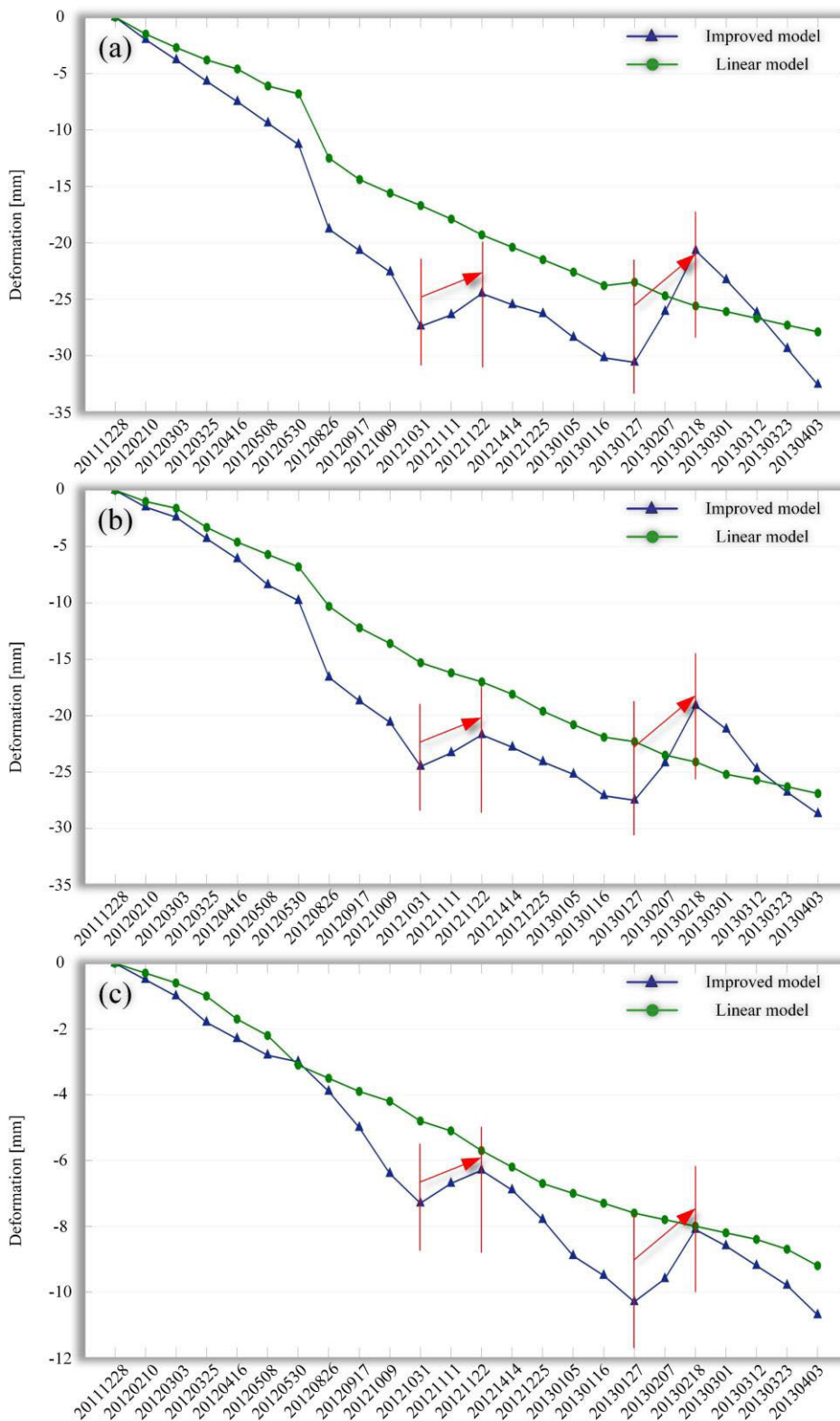


FIGURE 10. The optical images of feature points: (a) point A is located at the YH Avenue and closed to the Dongting Lake; (b) point B is located at the intersection of YH Avenue and Dongting Bridge; (c) point C is located at the intersection of X206 Road and Baling East Road; (d) point R is the reference point locates at the residential area.

between the soil mass is, accordingly less strain and deformation. This is the key reason why the area with low deformation showed a higher magnitude of elastic modulus and viscosity.

To further analyze the rheological characteristics of this area, we draw the rheological curve according to the mechanism of the Maxwell model, which is shown as Fig. 12 [27]. The rheological curve describes the temporal variations for the strain  $\epsilon$  physically, which can help us to further understand the deformation mechanism for the soil material. It is widely used in the field of geotechnical engineering. As Fig. 12 shows, the stress-strain functional relationship can be expressed as  $\epsilon = \frac{\sigma_c}{E}$  at the moment  $t = 0$ , which is called instantaneous elastic deformation. This is the characteristic of a dashpot-spring multimer, which describes that at the

moment of loading, the spring will produce elastic deformation immediately. In the secondary consolidation stage of soft clay, the soil deformation consists of two temporal periods: the first period is time-dependent (shown as the 0 to  $t_1$  period when the deformation linearly increases with time), which is called the constant velocity creep, following the viscous flow function  $\epsilon = \frac{\sigma_c}{\eta}t$ ; the second period is the instantaneous elastic deformation, which is time-irrelevant but highly related to the nature of materials. At the moment of unloading (see Fig. 12 when  $t = t_1, \sigma = 0$ ), the instantaneous elastic deformation immediately recovers while the viscous flow part cannot be restored. During the operation step of the highway post-construction, the external load can be considered as a constant. Accordingly, we mainly focus on the rheological



**FIGURE 11.** Temporal evolution of deformation based on two models at three feature points (X-axis represents the acquisition dates of SAR images and Y-axis represents the InSAR-generated deformation): (a) Point A; (b) Point B; (c) Point C.

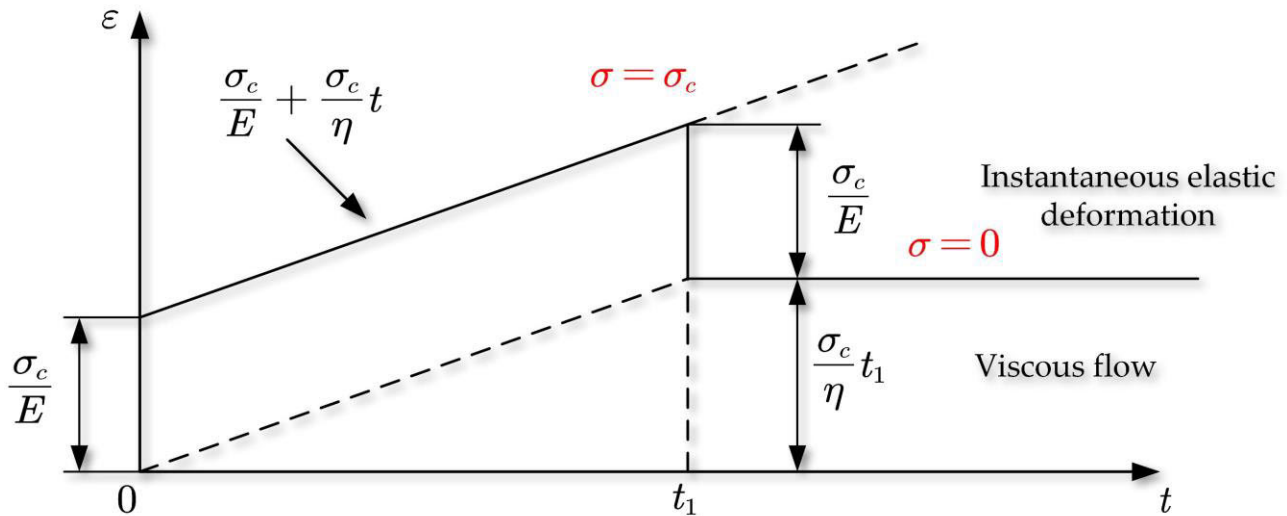


FIGURE 12. The rheological curve of the Maxwell model.



FIGURE 13. Monthly mean temperature and total precipitation from December 2011 to April 2013.

properties of the soil during the period of  $0 - t_1$ , when the external load was  $\sigma_c$ , and the strain was linearly varying with time ideally. Based on the aforementioned analysis on the rheological curve, the ideal strain can be estimated for each point in our test area. For the selected point A located in YH, the estimated elastic modulus and viscosity were 12.1 MPa and  $1.1 \times 10^6$  MPa.s, respectively. Its strain accumulated to 9.3 until April 2013. For point B, the estimated rheological parameters were 15.2 MPa and  $2.2 \times 10^6$  MPa.s, respectively. Its strain was estimated as 5.2 in April 2013. For point C, the estimated elastic modulus and viscosity were 26.3 MPa and  $7.2 \times 10^6$  MPa.s, respectively. Its strain was calculated as 1.4 in April 2013. It can be inferred that the estimated rheological parameters and the rheological curve can well reflect the rheological properties of materials with physical significance.

### C. SEASONAL FACTORS CONTRIBUTING TO SURFACE DEFORMATION

With the passage of time, when the natural compression of the soil reaches its limit and the porosity ratio drops to the minimum, the deformation caused by the initial external load and extravasation of the inner water in the soft soil ceases. Consequently, the subsequent deformation is mainly affected by external environmental factors. Quaternary deposits are largely distributed at the bank area of Dongting Lake with various thicknesses. The shallow groundwater possesses a certain relationship with the surface stream. As Fig. 13 shows, the precipitation of Yueyang City in November 2012 increased by 140 mm compared to that in October, whereas the temperature dropped by 10 °C (remarked as the first red arrow in Fig.13). With a combined impact of the increased precipitation and the drastically

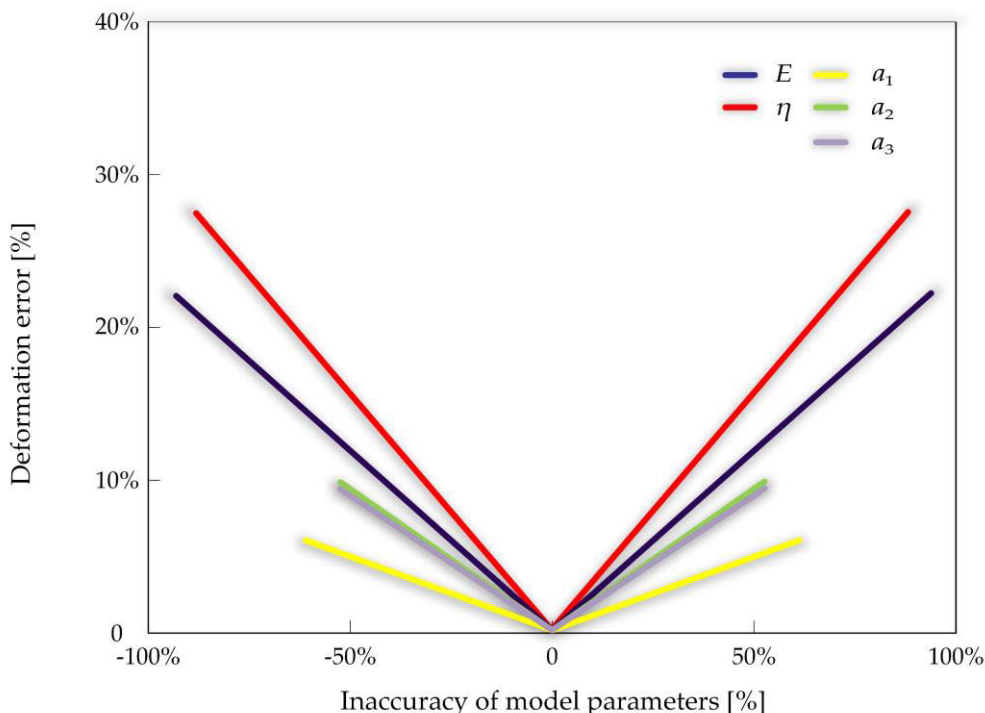


FIGURE 14. Results of sensitivity analysis for IM.

decreased temperature, the groundwater of the underground aquifer rose considerably due to the external recharge, which induced a surface uplift of 3 mm at point A (see the first red arrow shown in Fig. 11). Similarly, an increment of 170 mm’s precipitation occurred from February 2013 to January 2013 (remarked as the second red arrow in Fig. 13). Although with a constant temperature, the large increment of rainfall still resulted in a surface uplift of 10 mm at point A (see the second red arrow in Fig. 11). The quantitative results showed that the magnitude of uplift from January 2013 to February 2013 was higher than that from October 2012 to December 2012, which inferred that the effect of a rise in precipitation on surface uplift showed greater impact than that of temperature.

**D. SENSITIVITY ANALYSIS FOR IM**

As discussed in reference [51], the accuracies of the deformations acquired by the InSAR deformation model mainly depend on the accuracies of the estimated model parameters. If the estimated deformation is highly sensitive to a certain parameter, the final deformation will change greatly with a slight error of the parameter. For those insensitive parameters, even a large error occurred, the deformation results will not be affected. Hence, it is imperative to conduct a sensitivity analysis between the IM parameters and the estimated deformation using simulated data. According to the procedures introduced in [45], eight groups of inaccurate parameters were used as input data to generate the final deformation. TABLE 7 shows the simulated values of the five parameters and the ranges of the errors for each model parameter. The corresponding

TABLE 7. Analytical ranges and simulated inaccuracy of the IM parameters.

Parameters	<i>I</i>	Ranges of <i>I'</i>	Simulated inaccuracy
<i>E</i> (MPa)	25	0 - 50	-100% - 100%
$\eta$ ( $10^6$ MPa.s)	5	0 - 10	-100% - 100%
<i>a</i> <sub>1</sub> (m/yr)	-60	-100 - 20	-67% - 67%
<i>a</i> <sub>2</sub> (m/yr)	-10	-15 - 5	-50% - 50%
<i>a</i> <sub>3</sub> (m/yr)	-10	-15 - 5	-50% - 50%

simulated inaccuracy was defined according to the function:  $\frac{(I'-I)}{I} \times 100\%$ .

Fig. 14 shows the sensitivity analysis results compared for IM, which demonstrates the resulting errors of the estimated vertical subsidence *S* induced by the simulated inaccuracy of the model parameters. The resulting error of the vertical deformation *S* was defined by  $\frac{S}{S_{max}} \times 100\%$ , where *S*<sub>max</sub> denoted the maximum subsidence in its region. As Fig. 14 shows, the deformation error due to inaccurate model parameters was always symmetric in positive and negative directions. The IM-estimated vertical deformation was highly sensitive to the parameters  $\eta$  and *E*. In contrast, the influences of model parameters *a*<sub>1</sub>, *a*<sub>2</sub>, and *a*<sub>3</sub> were much limited. The result of the analysis is consistent with the discussions in VI-A, that the rheological deformation component performed a much higher effect than the seasonal component. Consequently, it is crucial to accurately estimate the highly sensitive parameters  $\eta$  and *E*.

## VII. CONCLUSION

In this work, the time series surface deformation over a soft soil area near Dongting Lake was investigated with the use of SBAS-InSAR technology and TerraSAR-X imaginary. Considering the deficiency of the traditional deformation models, an improved model, based on the functional relationship between strain and time in Maxwell rheological model, was proposed in InSAR deformation modeling. The rheological parameters of elastic modulus and viscosity were introduced into a traditional empirical seasonal periodical model. The rheological parameters were estimated through GA, and the time series deformation was inverted over a soft clay highway (YH highway) and the nearby area around Dongting Lake eventually. Through the analysis of the generated results, we found that the lower the viscosity and elastic modulus were, the higher the deformation was. Temporally, two seasonal uplifts with the maximum subsidence recovery of 5 mm from October 2012 to December 2012 and 12 mm from January 2013 to February 2013 were detected. The suggested reason for the fluctuation was related to a sudden rise in precipitation and a decrease in temperature.

To compensate for the deficiency of the unavailability of external geodetic measurements over this area, three different accuracy indexes (residual phase, temporal coherence, and HP deformation) were utilized to evaluate the accuracy. A comparative analysis based on four different types of deformation models, including the conventional Linear Model (LM), the Cubic Polynomial Model (CPM), the Seasonal Model (SM), and the Improved Model (IM), was executed to reflect the effect of the improved model. The final results for the three indexes showed that the IM was highly recommended with its better accuracy. We also carried out a sensitivity analysis between the IM parameters and the generated subsidence, which suggested that the accuracy of the IM-generated vertical subsidence was highly sensitive to elastic modulus  $E$  and viscosity  $\eta$ .

In this work, only the internal physical factor and seasonal environmental factors were considered for the observed objects. In the future study, we will focus on introducing specific climate factors (such as temperature, precipitation, and humidity) into the InSAR deformation modeling.

## AUTHOR CONTRIBUTIONS

X.X. designed the experiment. Y.Z. carried out the experiment. X.X. and Y.Z. analyzed the experiment results. L.B., L.Z., L.C., and Z.Y. participated in the discussion of the experimental conclusion. Y.Z. wrote the manuscript of the paper. All the authors contributed to the revision of the manuscript, reviewed and approved the manuscript.

## ADDITIONAL INFORMATION

Competing Interests: The authors declare no competing interests.

## ACKNOWLEDGMENT

The TerraSAR-X satellite images used in this paper are provided by the German Space Center (DLR) (Data Order Program Project: MTH3393, MTH3728).

## REFERENCES

- [1] J. Xia, G.-L. Huang, and S.-B. Yan, "Behaviour and engineering implications of recent floodplain soft soil along lower reaches of the Yangtze river in Western Nanjing, China," *Eng. Geol.*, vol. 87, nos. 1–2, pp. 48–59, Sep. 2006, doi: [10.1016/j.enggeo.2006.05.006](https://doi.org/10.1016/j.enggeo.2006.05.006).
- [2] A. Hooper, "A multi-temporal InSAR method incorporating both persistent scatterer and small baseline approaches," *Geophys. Res. Lett.*, vol. 35, no. 16, pp. 203–296, Aug. 2008, doi: [10.1029/2008GL034654](https://doi.org/10.1029/2008GL034654).
- [3] X. Shi, M. Liao, T. Wang, L. Zhang, W. Shan, and C. Wang, "Expressway deformation mapping using high-resolution TerraSAR-X images," *Remote Sens. Lett.*, vol. 5, no. 2, pp. 194–203, Feb. 2014, doi: [10.1080/2150704X.2014.891774](https://doi.org/10.1080/2150704X.2014.891774).
- [4] A. Ferretti, C. Prati, and F. Rocca, "Permanent scatterers in SAR interferometry," *IEEE Trans. Geosci. Remote Sens.*, vol. 39, no. 1, pp. 8–20, Jan. 2001, doi: [10.1109/36.898661](https://doi.org/10.1109/36.898661).
- [5] P. Berardino, G. Fornaro, R. Lanari, and E. Sansosti, "A new algorithm for surface deformation monitoring based on small baseline differential SAR interferograms," *IEEE Trans. Geosci. Remote Sens.*, vol. 40, no. 11, pp. 2375–2383, Nov. 2002, doi: [10.1109/TGRS.2002.803792](https://doi.org/10.1109/TGRS.2002.803792).
- [6] L. Bateson, F. Cigna, D. Boon, and A. Sowter, "The application of the intermittent SBAS (ISBAS) InSAR method to the South Wales Coalfield, UK," *Int. J. Appl. Earth Observ. Geoinf.*, vol. 34, pp. 249–257, Feb. 2015, doi: [10.1016/j.jag.2014.08.018](https://doi.org/10.1016/j.jag.2014.08.018).
- [7] L. Zhang, Z. Lu, X. Ding, H.-S. Jung, G. Feng, and C.-W. Lee, "Mapping ground surface deformation using temporarily coherent point SAR interferometry: Application to los angeles basin," *Remote Sens. Environ.*, vol. 117, pp. 429–439, Feb. 2012, doi: [10.1016/j.rse.2011.10.020](https://doi.org/10.1016/j.rse.2011.10.020).
- [8] Z. Du, L. Ge, A. H. M. Ng, Q. Zhang, and M. M. Alamdari, "Assessment of the accuracy among the common persistent scatterer and distributed scatterer based on SqueeSAR method," *IEEE Geosci. Remote Sens. Lett.*, vol. 15, no. 12, pp. 199–209, Dec. 2018, doi: [10.1109/LGRS.2018.2864274](https://doi.org/10.1109/LGRS.2018.2864274).
- [9] F. Chen, H. Lin, Z. Li, Q. Chen, and J. Zhou, "Interaction between permafrost and infrastructure along the Qinghai—Tibet railway detected via jointly analysis of C- and L-band small baseline SAR interferometry," *Remote Sens. Environ.*, vol. 123, pp. 532–540, Aug. 2012, doi: [10.1016/j.rse.2012.04.020](https://doi.org/10.1016/j.rse.2012.04.020).
- [10] M. Crosetto, O. Monserrat, M. Cuevas-González, N. Devanthéry, G. Luzi, and B. Crippa, "Measuring thermal expansion using X-band persistent scatterer interferometry," *ISPRS J. Photogramm. Remote Sens.*, vol. 100, pp. 84–91, Feb. 2015, doi: [10.1016/j.isprsjprs.2014.05.006](https://doi.org/10.1016/j.isprsjprs.2014.05.006).
- [11] D. Perissin, Z. Wang, and H. Lin, "Shanghai subway tunnels and highways monitoring through cosmo-skymed persistent scatterers," *ISPRS J. Photogramm. Remote Sens.*, vol. 73, pp. 58–67, Sep. 2012, doi: [10.1016/j.isprsjprs.2012.07.002](https://doi.org/10.1016/j.isprsjprs.2012.07.002).
- [12] P. Ma, T. Li, C. Fang, and H. Lin, "A tentative test for measuring the sub-millimeter settlement and uplift of a high-speed railway bridge using COSMO-skymed images," *ISPRS J. Photogramm. Remote Sens.*, vol. 155, pp. 1–12, Sep. 2019, doi: [10.1016/j.isprsjprs.2019.06.013](https://doi.org/10.1016/j.isprsjprs.2019.06.013).
- [13] Y. Zhang, H. A. Wu, and G. Sun, "Deformation model of time series interferometric SAR techniques," *Acta Geodaetica Cartogr. Sinica*, vol. 41, no. 6, pp. 864–869, Dec. 2012.
- [14] S.-W. Kim, S. Wdowinski, T. H. Dixon, F. Amelung, J. W. Kim, and J.-S. Won, "Measurements and predictions of subsidence induced by soil consolidation using persistent scatterer InSAR and a hyperbolic model," *Geophys. Res. Lett.*, vol. 37, no. 5, pp. 1–5, Mar. 2010, doi: [10.1029/2009GL014644](https://doi.org/10.1029/2009GL014644).
- [15] B. M. Kampes and R. F. Hanssen, "Ambiguity resolution for permanent scatterer interferometry," *IEEE Trans. Geosci. Remote Sens.*, vol. 42, no. 11, pp. 2446–2453, Nov. 2004, doi: [10.1109/TGRS.2004.835222](https://doi.org/10.1109/TGRS.2004.835222).
- [16] E. A. Hetland, P. Musé, M. Simons, Y. N. Lin, P. S. Agram, and C. J. DiCaprio, "Multiscale InSAR time series (MInTS) analysis of surface deformation," *J. Geophys. Res.-Solid Earth*, vol. 117, no. 2, pp. 1–17, Feb. 2012, doi: [10.1029/2011JB008731](https://doi.org/10.1029/2011JB008731).



- [17] R. Zhao, Z.-W. Li, G.-C. Feng, Q.-J. Wang, and J. Hu, "Monitoring surface deformation over permafrost with an improved SBAS-InSAR algorithm: With emphasis on climatic factors modeling," *Remote Sens. Environ.*, vol. 184, pp. 276–287, Oct. 2016, doi: [10.1016/j.rse.2016.07.019](https://doi.org/10.1016/j.rse.2016.07.019).
- [18] C. Wang, Z. Zhang, H. Zhang, Q. Wu, B. Zhang, and Y. Tang, "Seasonal deformation features on Qinghai-Tibet railway observed using time-series InSAR technique with high-resolution TerraSAR-X images," *Remote Sens. Lett.*, vol. 8, no. 1, pp. 1–10, Sep. 2016, doi: [10.1080/2150704X.2016.1225170](https://doi.org/10.1080/2150704X.2016.1225170).
- [19] Z. F. Yang, Z. W. Li, J. J. Zhu, J. Hu, and G. Feng, "Deriving dynamic subsidence of coal mining areas using InSAR and logistic model," *Remote Sens.*, vol. 9, pp. 1–19, Feb. 2017, doi: [10.3390/rs9020125](https://doi.org/10.3390/rs9020125).
- [20] X. Qin, L. Zhang, X. Ding, M. Liao, and M. Yang, "Mapping and characterizing thermal dilation of civil infrastructures with multi-temporal X-band synthetic aperture radar interferometry," *Remote Sens.*, vol. 10, pp. 1–22, Jun. 2018, doi: [10.3390/rs10060941](https://doi.org/10.3390/rs10060941).
- [21] Y. Zhu, X. Xing, L. Chen, Z. Yuan, and P. Tang, "Ground subsidence investigation in Fuoshan, China, based on SBAS-InSAR technology with TerraSAR-X images," *Appl. Sci.*, vol. 9, no. 10, p. 2038, May 2019, doi: [10.3390/app9102038](https://doi.org/10.3390/app9102038).
- [22] D. A. Sun and G. E. Shen, "Experimental study on rheology behaviour of Shanghai soft clay," *Hydrogeol. Eng. Geol.*, vol. 37, no. 3, pp. 74–78, May 2010.
- [23] M. Sun, Q. Wang, C. Niu, H. Yan, J. Dong, G. Xiao, X. Xu, and T. Sun, "Rheological consolidation theory of soft soils with secondary consolidation effect," *J. Eng. Geol.*, vol. 23, no. 4, pp. 675–680, Aug. 2015, doi: [10.13544/j.cnki.jeg.2015.04.013](https://doi.org/10.13544/j.cnki.jeg.2015.04.013).
- [24] M.-Q. Sun, Q. Wang, C.-C. Niu, and T. Sun, "Research on the one-dimensional rheological consolidation theory that considers secondary consolidation effect," *J. Comput. Theor. Nanosci.*, vol. 13, no. 2, pp. 1136–1146, Feb. 2016, doi: [10.1166/jctn.2016.5024](https://doi.org/10.1166/jctn.2016.5024).
- [25] B. W. Zhao, *Consolidation and Rheology for Soft Clay*. Nanjing, China: Hohao Univ. Press, 1996.
- [26] T. R. Lauknes, H. A. Zebker, and Y. Larsen, "InSAR deformation time series using an  $L_1$ -norm small-baseline approach," *IEEE Trans. Geosci. Remote Sens.*, vol. 49, no. 1, pp. 536–546, Jan. 2011, doi: [10.1109/TGRS.2010.2051951](https://doi.org/10.1109/TGRS.2010.2051951).
- [27] M. K. Huang, *Highway Engineering Material Rheology*. Chengdu, China: Southwest Jiaotong Univ. Press, 2010.
- [28] S. You, Z. C. Zhang, and H. G. Ji, "A thermodynamic constitutive model for creep behavior of rocks and its application," *J. Chin. Univ. Min. Technol.*, vol. 45, no. 3, pp. 507–513, 2016.
- [29] S. S. Li, Z. W. Li, J. Hu, Q. Sun, and X. Y. Yu, "Investigation of the seasonal oscillation of the permafrost over Qinghai-Tibet Plateau with SBAS-InSAR algorithm," *Chin. Geophys.*, vol. 56, no. 5, pp. 1476–1486, May 2013.
- [30] C. Colesanti, A. Ferretti, F. Novali, C. Prati, and F. Rocca, "SAR monitoring of progressive and seasonal ground deformation using the permanent scatterers technique," *IEEE Trans. Geosci. Remote Sens.*, vol. 41, no. 7, pp. 1685–1701, Jul. 2003, doi: [10.1109/TGRS.2003.813278](https://doi.org/10.1109/TGRS.2003.813278).
- [31] L. Liu, Q. Yan, and H. Sun, "A study on model of rheological property of soft clay," *Rock Soil Mech.*, vol. 27, no. suppl., pp. 214–217, Oct. 2006.
- [32] G. R. Liu, X. Han, and K. Y. Lam, "A combined genetic algorithm and nonlinear least squares method for material characterization using elastic waves," *Comput. Method. Appl. Mech. Eng.*, vol. 191, nos. 17–18, pp. 1909–1921, Feb. 2002, doi: [10.1016/S0045-7825\(01\)00359-0](https://doi.org/10.1016/S0045-7825(01)00359-0).
- [33] W. Long, P. Cheng, J. Zhao, J. Luo, and Z. Wang, "Comparative study on reinforcing soft soil treatment program in Dongting Lake area," *Explor. Eng.*, vol. 37, no. 9, Mar. 2010.
- [34] J. N. Wu, "Discussion on geological properties of soft soil in Dongting Lake area," *J. Central South Highway Eng.*, vol. 29, no. 2, pp. 136–138, Jun. 2004.
- [35] R. Q. Zhang, X. Liang, G. L. Zhang, and J. G. Pi, "A preliminary study of climatic change in Dongting lake area in the quaternary period," *Geol. Sci. Technol. Inf.*, vol. 20, no. 2, pp. 1–5, 2001.
- [36] E. Brawner, "Synthetic aperture radar interferometry analysis of ground deformation within the Coso geothermal site, California," M.S. thesis, Dept. Eng., Univ. Arkansas, Batesville, AR, USA, May 2016.
- [37] *Precipitation and Temperature Data of Yueyang City, China*. Accessed: Jun. 13, 2011. [Online]. Available: <http://www.tianqi.911cha.com/yueyang/2012>
- [38] M. Costantini and P. A. Rosen, "A generalized phase unwrapping approach for sparse data," in *Proc. IEEE Int. Geosci. Remote Sens. Symp.*, Jun/Jul. 1999, pp. 267–269.
- [39] X. Xing, D. Wen, H.-C. Chang, L. F. Chen, and Z. H. Yuan, "Highway deformation monitoring based on an integrated CRInSAR algorithm—Simulation and real data validation," *Int. J. Pattern Recognit. Artif. Intell.*, vol. 32, no. 11, Nov. 2018, Art. no. 1850036, doi: [10.1142/S0218001418500362](https://doi.org/10.1142/S0218001418500362).
- [40] T. Spałek, P. Pietrzyk, and Z. Sojka, "Application of the genetic algorithm joint with the powell method to nonlinear least-squares fitting of powder EPR spectra," *J. Chem. Inf. Model.*, vol. 45, no. 1, pp. 18–29, Jan. 2005, doi: [10.1021/ci049863s](https://doi.org/10.1021/ci049863s).
- [41] L. Yao and W. A. Sethares, "Nonlinear parameter estimation via the genetic algorithm," *IEEE Trans. Signal Process.*, vol. 42, no. 4, pp. 927–935, Apr. 1994, doi: [10.1109/78.285655](https://doi.org/10.1109/78.285655).
- [42] J. Ju, "Analysis on engineering geological problems along embankment in the middle and lower reaches of Yangtze river," *Chin. J. Geol. Hazards Control*, vol. 12, no. 2, pp. 23–25, Jun. 2001, doi: [10.3969/j.issn.1003-8035.2001.02.004](https://doi.org/10.3969/j.issn.1003-8035.2001.02.004).
- [43] Z. Deng, Z. Zhu, X. Zeng, and G. Kong, "Study on rheological properties of the lacustrine soft soil under different stress level," *Ind. Const.*, vol. 44, no. 6, pp. 67–72, Jan. 2014, doi: [10.13204/j.gyjz201406016](https://doi.org/10.13204/j.gyjz201406016).
- [44] Z. Mo, "The research on settlement analysis and monitoring of soft soil foundation in Port road," M.S. thesis, Dept. Transp. Eng., Changsha Univ. Sci. Technol., Changsha, China, 2012.
- [45] L. Xiao, "Study on rheological characteristics of lacustrine soil in Dongting Lake area," M.S. thesis, Dept. Civil Eng., Hunan Univ. Sci. Technol., Zhuzhou, China, 2018.
- [46] X. M. Xing, L. F. Chen, Z. H. Yuan, and Z. N. Shi, "An improved time-series model considering rheological parameters for surface deformation monitoring of soft clay subgrade," *Sensors*, vol. 19, no. 14, p. 3073, Jul. 2019, doi: [10.3390/s19143073](https://doi.org/10.3390/s19143073).
- [47] I. Armas, D. A. Mendes, R.-G. Popa, M. Gheorghie, and D. Popovici, "Long-term ground deformation patterns of Bucharest using multi-temporal InSAR and multivariate dynamic analyses: A possible transpressional system?" *Sci. Rep.*, vol. 7, no. 1, p. 43762, Mar. 2017.
- [48] S. S. Shi, "Shear strength, modulus of rigidity and Young's modulus of concrete," (in Chinese), *Chin. Civil Eng. J.*, vol. 32, no. 2, pp. 47–52, Apr. 1999.
- [49] F. He, C. E. Woods, J. R. Litowski, L. A. Roschen, H. S. Gadgil, V. I. Razinkov, and B. A. Kerwin, "Effect of sugar molecules on the viscosity of high concentration monoclonal antibody solutions," *Pharmaceutical Res.*, vol. 28, no. 7, pp. 1552–1560, May 2011.
- [50] F. Xiangjun, "Viscosity (rigidity coefficient) of high concentration turbid water," *J. Hydraul. Eng.*, vol. 3, no. 1, pp. 59–65, Oct. 1982.
- [51] Z. Yang, Z. Li, J. Zhu, A. Preusse, J. Hu, G. Feng, Y. Wang, and M. Papst, "An InSAR-based temporal probability integral method and its application for predicting mining-induced dynamic deformations and assessing progressive damage to surface buildings," *IEEE J. Sel. Topics Appl. Earth Observ. Remote Sens.*, vol. 11, no. 2, pp. 472–484, Feb. 2018.
- [52] F. Cannavò, "Sensitivity analysis for volcanic source modeling quality assessment and model selection," *Comput. Geosci.*, vol. 44, pp. 52–59, Jul. 2012, doi: [10.1016/j.cageo.2012.03.008](https://doi.org/10.1016/j.cageo.2012.03.008).



**YIKAI ZHU** was born in Hunan, China, in 1997. He received the B.S. degree in geomatics and surveying from the Changsha University of Science and Technology, Changsha, China, in 2018. He will receive the M.S. degree, in 2021.

His research interests include the application of the time series InSAR technique in highways deformation monitoring.



**XUEMIN XING** was born in Liaoning, China, in 1983. She received the B.S. and M.S. degrees and the Ph.D. degree in geomatics and surveying from Central South University, Changsha, China, in 2005, 2008, and 2011, respectively.

From 2016 to 2017, she was a Visiting Scholar with the Department of Environmental Sciences, Macquarie University, Sydney, NSW, Australia. She is currently an Associate Professor with the School of Traffic and Transportation Engineering,

Changsha University of Science and Technology, Changsha, where she is also a Key Member of the Laboratory of Radar Remote Sensing Applications. She is also a reviewer for three international journals and four national journals in China. She has authored more than 40 articles and ten inventions. Her research interests include the application of time-series interferometric synthetic aperture radar (InSAR) technique in highway deformation monitoring, deriving spatial-temporal large-scale deformation induced by mining activities and modeling, and the integration of persistent scatterer (PS), corner reflector (CR), and small baseline subset (SBAS) technique.



**ZHIHUI YUAN** (Member, IEEE) was born in Hunan, China, in 1983. He received the B.S. degree in electronic information engineering from Xiangtan University, Xiangtan, China, in 2007, and the Ph.D. degree in communication and information systems from the Institute of Electronics, Chinese Academy of Sciences, Beijing, China, in 2013.

Since 2013, he has been a Lecturer with the School of Electrical and Information Engineering, Changsha University of Science and Technology, Changsha, China. From 2018 to 2019, he was a Visiting Scholar with the Roy M. Huffington Department of Earth Sciences, Southern Methodist University, Dallas, TX, USA, working with Prof. Z. Lu on the interferometric synthetic aperture radar (InSAR) technique. He is also a Principal Investigator of the scientific project Research on Multichannel InSAR Robust DEM Inversion with High Precision for Complicated Terrain supported by the National Natural Science Foundation of China. His research interests include signal processing and the application of synthetic aperture radar interferometry, phase unwrapping, high-resolution digital elevation model generation, and algorithm design.

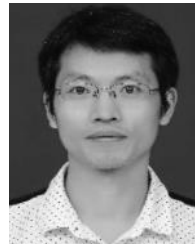


**LIANG BAO** was born in Hubei, China, in 1995. He received the B.S. degree from the Changsha University of Science and Technology, Changsha, China, in 2018, where he will receive the M.S. degree, in 2021.

His research mainly focuses on the application of the time series InSAR technique in bridges deformation monitoring.



**LINGJIE ZHU** was born in Hunan, China, in 1996. He received the B.S. degree from the Changsha University of Science and Technology, Changsha, China, in 2019. He will receive the M.S. degree from the Changsha University of Science and Technology, in 2022. His research mainly focuses on the application of the time series InSAR technique in highways deformation monitoring.



**LIFU CHEN** was born in 1979. He received the B.S. degree in electronic information engineering from Beihang University, Beijing, China, in 2007, and the Ph.D. degree in communication and information systems from the Institute of Electronics, Chinese Academy of Sciences, Beijing, in 2011.

Since 2011, he has been a Lecturer with the School of Electrical and Information Engineering, Changsha University of Science and Technology, Changsha, China. From August 2018 to August 2019, he was a Visiting Scholar with the School of Engineering, Newcastle University, Newcastle upon Tyne, U.K., working with Prof. Z. Li on AI in synthetic aperture radar (SAR)/interferometric SAR (InSAR) images. He is a Principal Investigator of the Scientific Project Research on Real-Time DEM Reconstruction with High Precision Using Airborne InSAR System supported by the National Natural Science Foundation of China. He has authored more than 40 articles. His research interests include SAR/InSAR signal processing, targets detection, and terrain classification for SAR/InSAR image with deep learning (landslide detection, classification for remote sensing images, extraction of water, and shadow and layover from InSAR images).

• • •